Novel interfacial lateral electron migration pathway formed by constructing metallized CoP$_2$/CdS interface for excellent photocatalytic hydrogen production

Xiangdong Xue [a], Wenjun Dong [a,*], Qingjie Luan [a], Hongyi Gao [a,b,**], Ge Wang [a,b,**]

[a] *Beijing Advanced Innovation Center for Materials Genome Engineering, Beijing Key Laboratory of Function Materials for Molecule & Structure Construction, School of Materials Science and Engineering, University of Science and Technology Beijing, Beijing 100083, PR China*
[b] *Shunde Graduate School, University of Science and Technology Beijing, Shunde 528399, PR China*

ABSTRACT

Promoting photo-induced electron transfer is one of the most efficient approaches for improving photocatalytic hydrogen production performance. Herein, we construct a novel interfacial lateral electron migration path by introducing CoP$_2$ into CdS photocatalytic system as cocatalyst for the first time. This peculiar migration path can be attributed to two aspects: 1) the built-in electric field between CoP$_2$ and CdS could drive carrier separation effectively; 2) the "metallized" interface serves as a special electron trap to accumulate electrons and promote them transfer along it instead of diffusion into cocatalyst. The energy-efficient interface shortens the electron migration distance and make more hot electrons participate in the reaction at the active sites with lower activation energy. As expected, the optimal hydrogen production rate of CoP$_2$/CdS reaches up to 1071 mmol h^{-1} g^{-1}, which is one of the most robust photocatalytic hydrogen production systems.

1. Introduction

With the deterioration of environment and the increasing demand for energy, it is of prime urgency to develop a renewable clean energy. Hydrogen energy, as the most potential alternative of fossil fuels, has been widely concerned. In recent years, the conversion of solar energy to hydrogen energy has been studied worldwide due to its green and sustainable characteristics [1–8]. As the core of photocatalytic system, photocatalyst determines the conversion efficiency of solar energy to hydrogen energy, therefore, rational design of the photocatalyst is crucial to enhance the hydrogen production performance [9–11]. Due to the photocatalytic process mainly occurs at surface/interface of the catalyst, the surface/interface engineering is a hot spot in current research [12–15]. Many groups have developed various schemes to design photocatalysts, including heterojunction forming [16,17], morphology controlling [18,19], cocatalyst loading [20,21] and surface defect engineering [22,23]. The essence of above strategy is a surface/interface related question. Among those, cocatalyst loading is a powerful tool of surface/interface engineering, which can efficiently promote carrier separation and accelerate surface reaction kinetics as much as possible without affecting the generation of electron-hole pairs.

Composed of earth-abundant elements, transition metal phosphides owning to stability, low cost and excellent activity has been widely studied as cocatalyst in recent years [24–27]. Among them, cobalt phosphide (CoP) and cobalt-rich cobalt phosphide (Co$_2$P) have been developed as the most promising alternatives to noble metals. For instance, Dong et al. [28] developed a novel photochemical strategy to synthesize Co$_x$P (x = 1–2), the optimized hydrogen evolution rate is about 500 mmol h^{-1} g^{-1} under visible light. Ao et al. [29] constructed CoP-CdS nanorods hybrid composites via a two-step in-situ growth method, the optimum hydrogen evolution rate was 9.11 times higher than that of pristine CdS. Yang et al. [30] designed a "ball-in-ball" core-shell structure with core of CoP loaded CdS and SiO$_2$ shell. The unique nano-photoreactor is beneficial to enhance hydrogen production activity by means of visible light multi-scattering effect as well as reagent enrichment effect. Fu et al. [31]. constructed CoP-CdS photocatalytic system, the hydrogen-production rate can reach up to 254 mmol h^{-1} g^{-1} under sunlight light irradiation. Xie et al. [32]

investigated the electron transfer behavior of CdS to Co_2P in detail by spectroscopic characterizations and theoretical calculations. In a more recent paper [33], density functional theory (DFT) calculations reveal that the high P content in CoP_2 both physically separates Co atoms to prevent H from over binding to multiple Co atoms, while simultaneously stabilizing H adsorbed to single Co atoms, resulting in an absolute free energy of hydrogen adsorption of almost 0 eV, that is critical for enhance surface reaction kinetics.

Although there are excellent works as mentioned above, the electrons need to cross the interface and diffuse through the cocatalyst to participate in the reaction [9–11] (Scheme 1b). Long diffusion path will lead to unnecessary energy loss. Furthermore, compared to the surface atoms of cocatalyst, because of the stronger dislocation, the average energy of interface atoms will increase, which will lower the activation energy for the hydrogen evolution. Therefore, directing the hot electrons to the interface will help to make better use of these "energy-saving" active sites. From this point of view, taking CoP_2/CdS NRs hybrid as a case, employing multiple characterization and DFT based first-principles calculation, we construct a new electron diffusion path. In the new path, the "metallized" interface between CoP_2 and CdS NRs serves as an electron trap, making the electrons accumulate at the interface and diffuse outward along it directly instead of into the cocatalyst (Scheme 1c). By means of this special interface, we could achieve the goals of shortening the electron transfer distance, promoting charge carrier separation and transportation, making more hot electrons flow to the active sites with lower activation energy, and then reducing the energy consumption. As expected, the optimized CoP_2/CdS NRs hybrid showed an excellent hydrogen production activity (1071 mmol h^{-1} g^{-1}), which is almost 77 folds to that of pristine CdS NRs, the apparent quantum yield (A.Q.Y.) at 420 nm is reach up to 12 %, which is a remarkable enhancement compared to that of pristine CdS NRs (A.Q.Y. at 420 nm is 0.07 %). Our work opens the doorway for the utilization of CoP_2 as an excellent hydrogen production cocatalyst, giving an idea that the suitable interface structure can greatly promote the photocatalytic hydrogen production.

2. Experimental section

2.1. Chemical and materials

All reagents are analytical reagent (A.R.) grade (purity ≥ 99.7 %) and used without any purification. Cadmium acetate dihydrate (Cd$(OAc)_2·2H_2O$) and Sodium hypophosphite (NaH$_2$PO$_2$) were obtained from Aladdin Industrial Inc., thiourea (NH$_2$CSNH$_2$) was obtained from Tianjin Jinke Fine Chemical Research Institute, ethylenediamine (C$_2$H$_4$(NH$_2$)$_2$) and ammonia solution (NH$_4$OH) was obtained from Sinopharm Chemical Reagent Co., Ltd. (Shanghai, China) and cobalt(II) acetate tetrahydrate (Co(OAc)$_2$·4H$_2$O) was purchased from Tianjin Guangfu Fine Chemical Research Institute.

2.2. Preparation

CoP_2/CdS NRs hybrids are labeled as Cox-Py, which are synthesized by a facile three-step method (where x represents the molar ratio of Co source/CdS, y represents the weight of P source. For instance, Co10-P50 is meant to that the molar ratio of Co source/CdS is 10 % and the weight of P source is 50 mg. Specially, Co0-P0 represents pure CdS NRs).

Here we take Co10-P50 as an example. Firstly, CdS nanorods was synthesized by a solvothermal process described in previous reports [29]. In short, 2.48 mmol Cadmium acetate dihydrate (Cd(OAc)$_2$·2H$_2$O) and 7.46 mmol thiourea (NH$_2$CSNH$_2$) were dispersed in 20 mL ethylenediamine (C$_2$H$_4$(NH$_2$)$_2$) and starred for half an hour, than the white product was transferred to a 30 mL Teflon-lined stainless-steel autoclave and heated at 180 °C for 24 h in an electric furnace. After cooling down to room temperature, the yellow precipitates were collected and washed with absolute ethanol and ultrapure water to remove any impurity. Secondly, 100 mg CdS NRs was dispersed in 60 mL ultra-pure water via starring for 1 h, then 0.069 mmol cobalt(II) acetate tetrahydrate (Co(OAc)$_2$·4 H$_2$O) was dispersed in the above solution and stirred for another 1 h, follow that we use the ammonia solution as precipitant to form Co(OH)$_2$ on the surface of CdS NRs, then the products were collected and washed with ultrapure water three times. Lastly, the precursor synthesized above was ground using a mortar with 50 mg sodium hypophosphite (NaH$_2$PO$_2$) then the mixture was putted into a tube furnace and heated at 300 °C for 2 h with a heating rate of 2 °C/min in Ar atmosphere. After cooling down to room temperature, the green products were washed using ultrapure water three times to remove any impurity.

CoP_2 was synthesized in the same way as Cox-Py, except that no CdS was added.

2.3. Characterization

Powder X-ray diffraction (XRD, Bruker D8 ADVANCE, Germany) with Cu- Kα radiation (1.5405 Å) was be used to measure the crystal structures of all the samples. The test is operated at 40 kV and 200 mA and the scanning rate was 10°/min with a step size of 0.02°. X-ray absorption fine structure (XAFS) spectra at Co K-edge were performed at 4B9A beamline of Beijing Synchrotron Radiation Facility (BSRF), China. The Extended X-ray absorption fine structure (EXAFS) data were disposed according to the standard procedures through the ATHENA module implemented in the IFEFFIT software packages. The k3-weighted χ(k) data in the k-space ranging from 3 to 13.5 Å^{-1} were Fourier transformed to real (R) space using a hanging window (dk = 1.0 Å^{-1}) to separate the EXAFS contributions from different coordination shells. The surface morphology of the materials is detected by a scanning electron microscopy (SEM, ZEISS SUPRA 55). For reveal the fine structures of the samples, Transmission electron microscopy (TEM, JEOL JEM1200EX) and high-resolution TEM (HRTEM, Titan ETEM G2
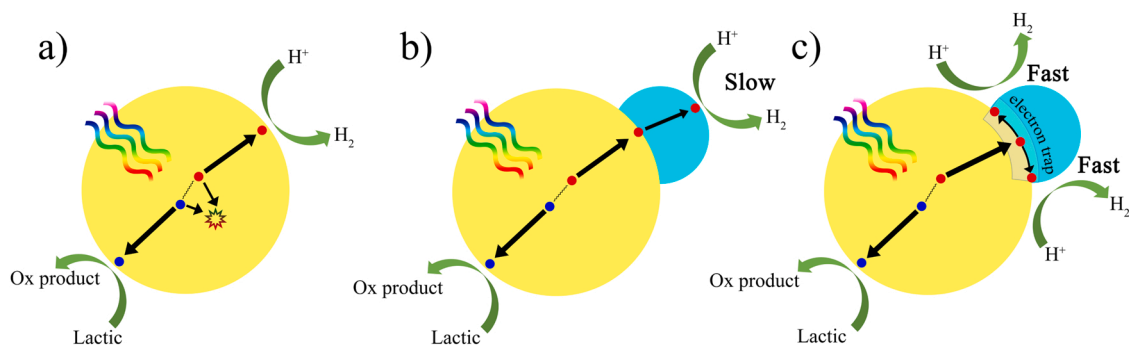
Scheme 1. Three possible carrier migration pathways of photocatalyst. a) without cocatalyst. b) with cocatalyst but the reaction take place in the surface of cocatalyst. c) with cocatalyst and the reaction take place in the interface between photocatalyst and cocatalyst. The red ball represents electrons and the blue one represents holes.

equipped with spherical aberration corrector) were employed. Element mapping analysis is conducted using energy-dispersive X-ray spectroscopy (EDS) which is equipped in HRTEM system. X-ray photoelectron spectroscopy (XPS) was performed to analyze the surface element states of the materials on a Thermo Scientific Escalab 250Xi system. To reveal the element composition of the samples, inductively coupled plasma optical emission spectrum (ICP-OES, Agilent ICPOES730) was applied. Ultraviolet-visible diffuse reflection spectra (UV-Vis DRS) were recorded on a Shimadzu UV-2550 spectrometer. The photoluminescence (PL) spectra for prepared samples were investigated by Edinburgh FL/FS900 spectrophotometer. The time resolved photoluminescence (TRPL) spectra were detected by a JY HORIBA FluoroLog-3 spectrometer.

2.4. Photocatalytic activity measurement

The photocatalytic hydrogen evolution tests were carried out in a 54.2 mL reactor at ambient conditions with stirring. A 300 W Xe lamp equipped with a UV cut-off filter ($\lambda > 420$ nm) was used as visible light source to trigger the whole reaction. 1.0 mg of as-prepared samples was dispersed in 20 mL of aqueous solution containing 5 mL L (+)-Lactic acid as sacrificial reagent, and then the suspension was stirred and pumped for 30 mins to fully degas. The evolved hydrogen gas was quantified by gas chromatography (Shimadzu GC-2014, Argon as carrier gas) using a 5 Å molecular sieve column and a thermal conductivity detector (TCD). The A.Q.Y. was simulated by the equation below:

$$A.Q.Y.(\%) = \frac{\text{number of reacted electrons}}{\text{number of incident photons}} \times 100\%$$
$$= \frac{\text{number of evolved H}_2 \text{ molecules} \times 2}{\text{number of incident photons}} \times 100\%$$

2.5. Photoelectrochemical measurement

To investigate the photoelectrochemical properties of materials, a standard three-electrode system (photocatalyst-covered FTO glass as working electrode, Pt wire as the counter electrode, Ag/AgCl as reference electrode and 0.5 M Na_2SO_4 as the electrolyte) was employed. A 300 W Xe lemp with a UV cut-off filter ($\lambda > 420$ nm) was utilized as the light source. The working electrodes were fabricated as follows: 10 mg as prepared solid was added into mixed solution made of Nafion and ethanol, then the slurry was dropped onto an FTO plate and the working electrodes were dried in an oven at 60 °C.

2.6. Computational method

Density functional theory (DFT) simulations were carried out using Cambridge Sequential Total Energy Package (CASTEP) module in Materials Studio software [34–36]. Perdew-Burke-Ernzerhof (PBE) version of the generalized gradient approximation (GGA) was employed to optimize the geometry structures of the models [37]. The ultrasoft pseudopotentials was used to simulate the interaction between valence electrons and ionic core [38]. An optimized 340 eV cut-off energy was be chosen to run all simulations. For hybrid model, a $1 \times 1 \times 1$ Monkhorst-Pack k-point grid was be set for Brillouin zone [39] since previous studies found that Γ point sampling of first Brillouin zone is sufficient to obtain correct electronic properties [40]. For all models, a vacuum space of 10 Å was built to avoid the interaction between neighbored layers. The convergence parameter for the electronic structure iteration were set as follows: 1.0×10^{-6} eV/atom for energy, 0.01 eV Å^{-1} for maximum force, 0.005 GPa for maximum pressure and 5×10^{-4} Å for maximum displacement. See supporting information for more details.

3. Result and discussion

3.1. Structural characterization

A series of Cox-Py complexes were synthesized by a three-step

strategy (Scheme 2). Firstly, CdS NRs was synthesized using a solvothermal method that has been widely reported in the literature [29]. And then different amounts of cobalt ions are deposited on the nanorods by successively adding a certain amount of cobalt acetate and ammonia. After that, the Co-containing intermediates were heated with different amounts of NaH_2PO_2 that served as the phosphorus source. Note that the ratio of cobalt to phosphorus in the product can be mediated simply by controlling the relative content of cobalt and phosphorus [41]. From the ICP-OES data (Table 1), the Co/P ratio of product decreases alone with the reduction of the content of Co source. Through hydrogen production tests (that will be analyzed in follow section), we found that Co10-P50 had the best hydrogen production performance, so we mainly analyzed the samples of Co10-P50 here. The EXAFS was used to illustrate the coordination structure of Co centers (Fig. 1a). The one dominant peak around 1.6 Å in Co10-P50 is attributed Co-P bond, which is different from the signal of Co-S bond and Co-Co bond, confirming that the existence of Cox-Py species as well as the absence of doped Co atoms (*see* supporting information *for more discussion*). Furthermore, the XRD results (*Fig.S1*) prove that the phosphorus is not doped in the lattice of cadmium sulfide even if the CdS NRs were annealed with the 50 mg phosphorus source only. Moreover, From the ICP-OES tests, the Co/P ratios in samples are regulated to 1, 1/2, and 1/3, respectively. For Co10-P50, it can be preliminarily determined that phosphorus exists in the form of CoP_2. To further confirm the conclusion, other means were used to determine the formation of CoP_2.

The morphology and element distribution of Co10-P50 hybrid photocatalyst were investigated by SEM, TEM, HRTEM and EDX-Mapping. The SEM images of CdS NRs (Fig. 2a, Fig. S2a) show that the prism-like CdS NRs with smooth surface were successfully prepared, which is consistent with previous reports [42]. After being modified, tiny nanoparticals with sizes of 10–20 nm appear on the surface of CdS NRs (Fig. 2b, Fig. S2b), indicating that Co10-P50 hybrid photocatalyst is successfully obtained. The TEM image of Co10-P50 hybrid sample (Fig. S2c) shows a detailed picture of its heterostructure. As for HRTEM results, from the top view of this heterostructure (Fig. 2c), there exists distinct lattice fringes stem from two compounds, lattice spacing of 0.336 nm and 0.211 nm is corresponding to the (002) plane and (110) plane of hexagonal CdS, respectively [42]; lattice spacing of nearly 0.265 nm, is corresponding to the (111) plane of monoclinic CoP_2 (Fig. S3, Fig. S4) [43]. Moreover, from a side view (Fig. 2e) there is clearly an order-disorder-order interface between two parts of this heterostructure with the interplanar spacing of 0.335 nm and 0.238 nm, which can be attributed to the (002) plane of CdS and {$\bar{1}$21} planes of CoP_2, respectively [42,43]. Combined with the above results, it can be determined that the small particles observed by SEM is CoP_2. Furthermore, through comparison with the theoretical models (Fig. 2d, Fig. 2f), it is further confirmed that CoP_2 is successfully prepared and the CoP_2 nanoparticals are tightly bound onto the surface of CdS nanorods with a specific orientation relationship, that is, the ($\bar{2}$02) plane of CoP_2 is combined with the (100) plane of CdS (Fig. 2g). Besides, the EDX-mapping results (Fig. S2d-h) show the existence Cd, S, P and Co, respectively, further implying the CoP_2 material were successfully loaded on the CdS NRs with fine dispersion. The content of the elements was determined by the more accurate ICP-OES (Table 1), in addition to the Co/P ratio mentioned earlier, the Co/Cd molar ratio was also calculated to be 0.02, which not only further explains the formation of CoP_2, but also detected the actual loading of CoP_2 (2 mol%).

The X-ray photoelectron spectroscopy (XPS) technique was employed to determine the composition and chemical states of Co10-P50 hybrid photocatalyst. In the high-resolution spectrum of Cd 3d and S 2p (Fig. 3a-b), two peaks of Cd 3d at 411.7 eV and 405 eV along with the two peaks of S 2p at 162.6 eV and 161.5 eV, are the nature of CdS [44]. For Co 2p core level (Fig. 3c), five main peaks could be observed in both Co10-P50 and CoP_2. For CoP_2, the peaks located at 777.9 eV and 792.8 eV are attributed to Co-P 2p$_{3/2}$ and Co-P 2p$_{1/2}$,
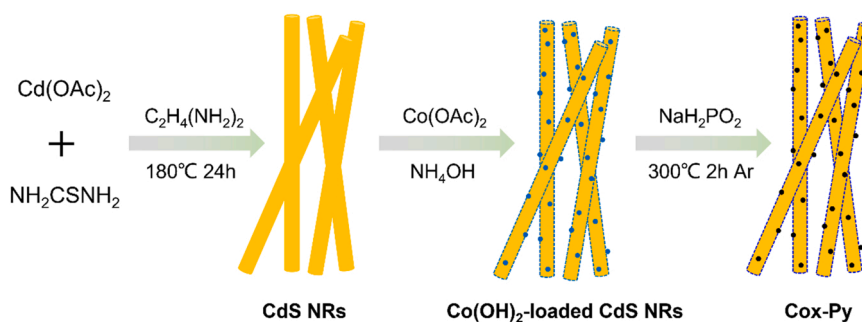
Scheme 2. The synthesis process of Cox-Py.

Table 1
The data from ICP-OES results of Cox-P50 (x = 5, 10, 20).

|	Items	wt %	mol%	Co/P molar ratio	Co/Cd molar ratio
Co20–50	Cd	77.6326013	50.66925617	1.002637404	0.045435288
	Co	1.84930077	2.302172229		
	P	0.969322765	2.296116443		
	S	19.54877517	44.73245515		
Co10–50	Cd	80.05416343	53.82854632	0.495955424	0.020497608
	Co	0.859876506	1.102794728		
	P	0.911167464	2.223576304		
	S	18.1747926	42.84508265		
Co5–50	Cd	79.78035472	53.28098761	0.375788796	0.015655635
	Co	0.654842395	0.834147709		
	P	0.915793854	2.219724797		
	S	18.64900903	43.66513989		
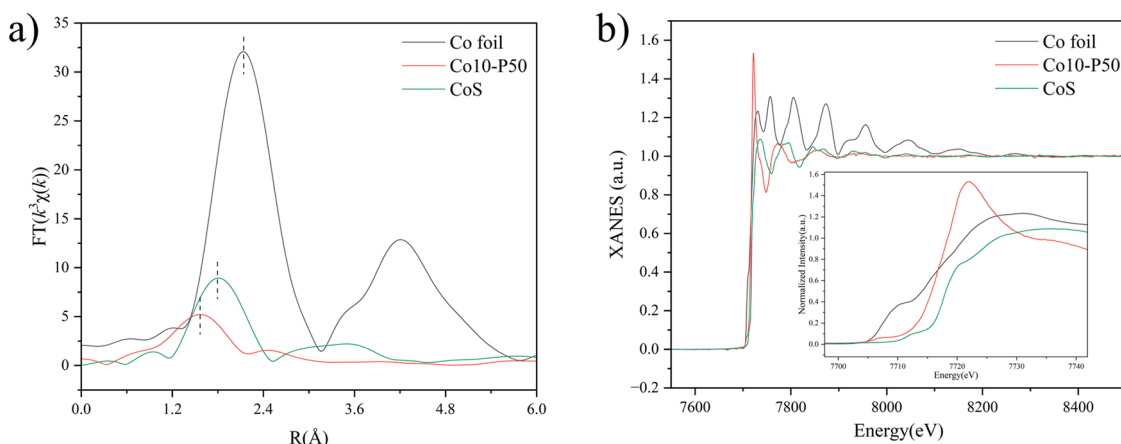
Fig. 1. a) Extended X-ray absorption fine structure and b) X-ray absorption near edge structure of Co10-P50.

respectively, which are typical characteristic peaks of CoP$_2$ [45]. Moreover, the XPS peaks of 781.1 eV and 797.6 eV are arised from Co-O, along with the satellite peak of 784.8 eV and 801.8 eV, are ineluctable because of the exposure in the air [45]. The peak located at 777.9 eV is slightly positively shifted from the metallic-state Co (777.8 eV), which is assigned to Co$^{\delta+}$. For P 2p (Fig. 3*d*), the peaks of CoP$_2$ at 128.7 eV and 129.5 eV are distributed to P 2p$_{3/2}$ and P 2p$_{1/2}$, respectively, which stem from Co-P in CoP$_2$ [45]. The peak at 133.7 eV come from P-O due to the superficial oxidation of CoP$_2$ in the air. The peak at 128.7 eV is negatively shifted from element P (130.2 eV), which is assigned to P$^{\delta-}$. The existence of Co$^{\delta+}$ and P$^{\delta-}$ implying the Co species possesses a partial positive charge and P species own a partial negative charge, that is a key evidence to prove the formation of CoP$_2$ due to the transfer of electron density from Co to P [45]. The same conclusion is proved further by X-ray absorption near edge structure (XANES) (Fig. 1*b*), in which the K edge of Co in Co10-P50 is slightly positive than Co foil but is negative

than CoS. Moreover, for Co10-P50, compare with CoP$_2$, the XPS peaks of Cd 3d didn't move, but the peaks of S 2p negatively shifted about 0.27 eV, while, the peaks of Co 2p and P 2p positively shifted about 0.2 eV and 0.3 eV, respectively, indicating that the electrons flow from CoP$_2$ to CdS NRs after the formation of heterogeneous interface [46]. It is worth noting that, like EXAFS, the XPS signal lacks the Co-S bond, see supporting information for detailed discussion.

3.2. Photocatalytic hydrogen production performance

Fig. 4*a* shows the H$_2$ evolution rate of Cox-Py photocatalysts. As a typical semiconducting photocatalyst, CdS NRs showed a certain photocatalytic activity for H$_2$ evolution but not efficient enough (~13.78 mmol h^{-1} g^{-1}). To rule out the effect of thermal treatment, the H$_2$ evolution performance of CdS NRs under the same heat treatment was also examined. The result shows that they have an analogous
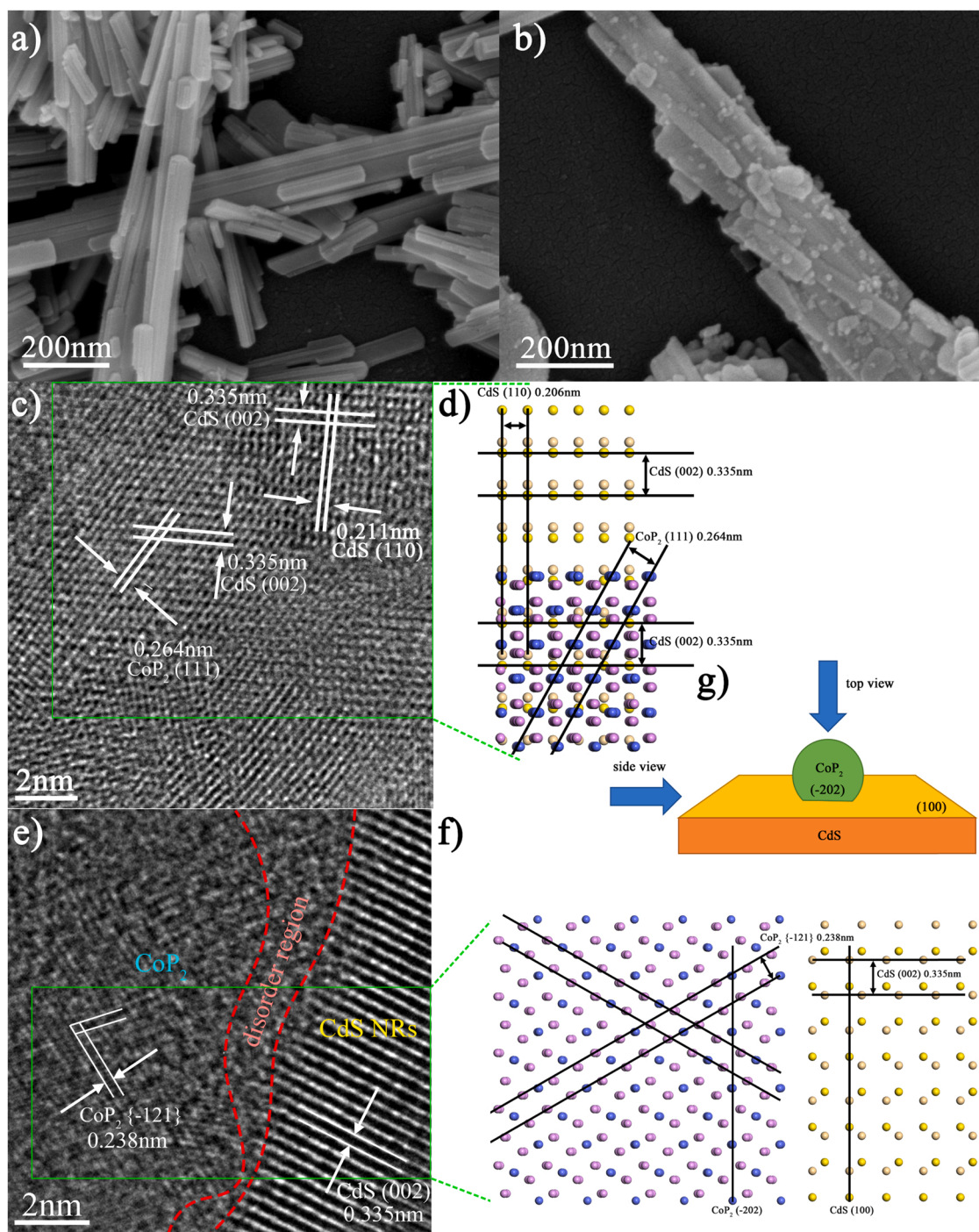
Fig. 2. SEM images of a) Co0-P0 and b) Co10-P50. HRTEM images of the interface between CoP_2 and CdS NRs, c) top view, e) side view. The corresponding theoretical models of the material in green box are represented in d) top view and f) side view, respectively. g) The illustration of viewing direction. Cd atoms, S atoms, Co atoms and P atoms are labeled as ochre, yellow, blue and purple spheres, respectively.

activity (*Fig.S5*), indicating the enhancement of photocatalytic activity for H_2 evolution don't stem from heat treatment. Moreover, CoP_2 itself does not have any hydrogen production capability (Fig. S5), indicating the nature of its co-catalyst. In addition, in the absence of Co or P element, the H_2 production performance of the samples is worse than that of pure CdS NRs, indicating that the presence of individual Co or P species is not beneficial to hydrogen production. To the contrary, with only a small amount of Co and P coexist on CdS NRs, its hydrogen production performance was dramatically enhanced up to ~114 mmol h^{-1} g^{-1} (the sample is Co5-P10). Obviously, different

proportions of Co and P endow the materials with different H_2 production capability. Note that for all the samples, the hydrogen production performance is highest only when the amount of Co source and P source meet a certain proportion (i.e., Co5–25, Co10–50 and Co20–100). Combined with the foregoing analysis about ICP-OES data and related paper [41], we could come to the conclusion that the performance boost could happen only when cobalt and phosphorus exist in the form of CoP_2. From another view of point, the more quantity of CoP_2 is not always better, a small amount of CoP_2 will have a positive impact on performance, but when it is more than a certain amount, CoP_2 will lead
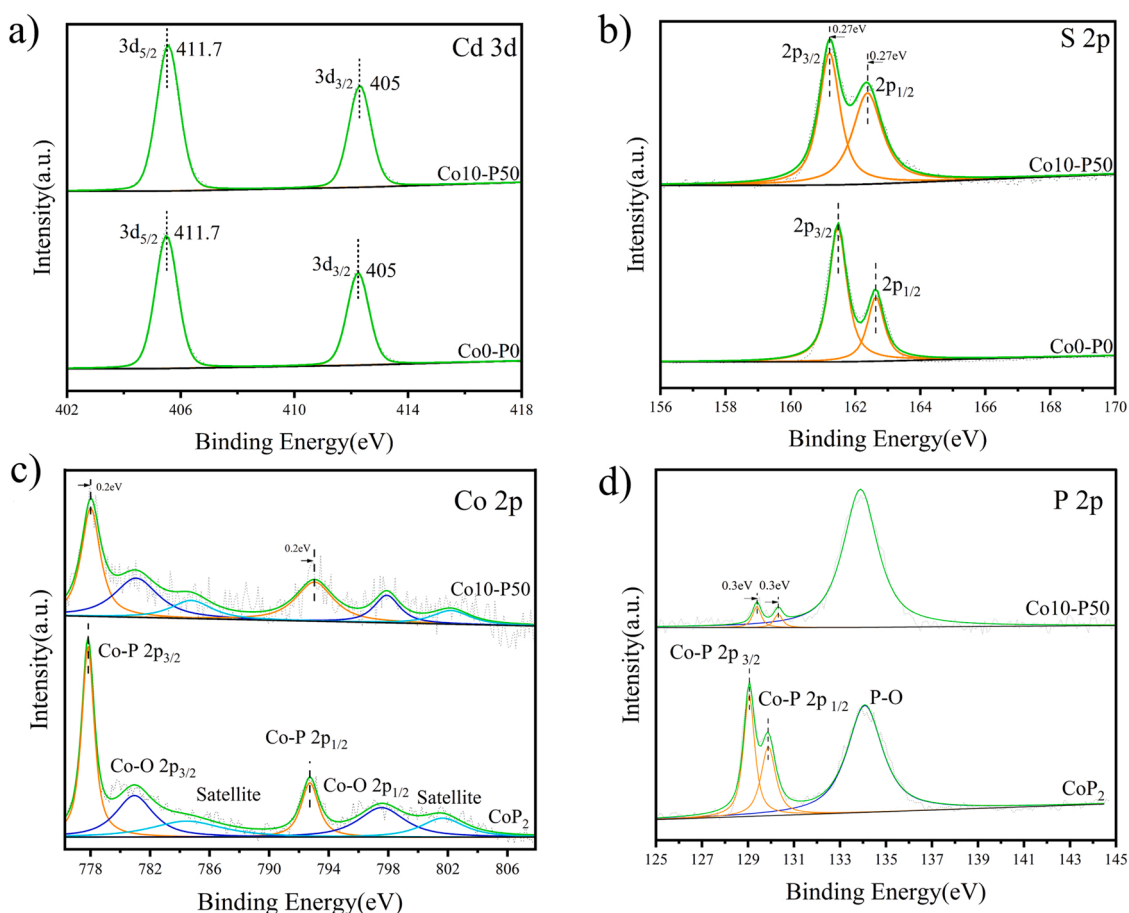
Fig. 3. High-resolution XPS spectra. a) Cd 3d of Co10-P50 and Co0-P0. b) S 2p of Co10-P50 and Co0-P0. c) Co 2p of Co10-P50 and CoP_2. d) P 2p of Co10-P50 and CoP_2.

to the degradation of hydrogen production performance. This may be due to the shielding effect and reduction of interface active sites caused by excessive CoP_2, which reduces the light absorption of CdS NRs and efficient use of hot electrons. As can be observed, the Co10-P50 have the highest hydrogen evolution rate (~1071 mmol $h^{-1}g^{-1}$), which is about 76 times higher than that of pristine CdS NRs, to our best knowledge, this value is the highest record compared with other Co_xP/CdS systems [28–32]. Fig. 4b shows the influence of lactic acid concentration to H_2 production performance. It's clear to see that the 25 v % lactic acid is most favorable for proton reduction, when lactic acid concentration comes to 50 v %, the efficiency of proton reduction is lower, it is probably due to excessive lactic acid hinders light absorption and proton absorption on the active sites. Fig. 4c represents the A.Q.Y. of Co10-P50 and Co0-P0 under 420 nm monochromatic light irradiation. The H_2 evolution rate of Co0-P0 was very low and corresponding A.Q.Y. was almost 0. Moreover, rapid deactivation of Co0-P0 was clearly observed, indicating that Co0-P0 is not suitable for industrial application. Conversely, the H_2 evolution rate of Co10-P50 was ~180 mmol $h^{-1} g^{-1}$ with an A.Q.Y. of nearly 12 % in 6 h. This fact illustrates that the CoP_2 in Co10-P50 hybrid photocatalyst not only enhance the photon utilization efficiency but also stabilize the CdS NRs. Stability is another key factor to scale the performance of photocatalysts. Herein, we tested the stability of Co10-P50 and Co0-P0 was used for comparison. The stability of Co0-P0 is very poor and the activity lasted about 2 h (Fig. 4d). After that, nearly no H_2 was produced. When it comes to Co10-P50, the activity maintains relatively high even after 25 h, indicating that CoP_2 can form stable heterostructure with CdS NRs.

3.3. Photocatalytic mechanism

To discover the possible reason for the remarkable enhancement of H_2 evolution rate and quantum yield of Co10-P50, the UV-Vis DRS technique was applied. From the original UV-Vis light absorption spectra (Fig. 5a, converted from diffuse reflectance spectra), the absorption level enhanced in both UV and visible region, especially in 500–800 nm region due to a narrow band gap of CoP_2. After Kubelka-Munk transformation (Fig. 5b), it's clear to see that the band gap of CdS NRs is 2.43 eV, which is consistent with previous studies [28–31], and for Co10-P50, the band gap is almost unchanged, indicating that Co and P formed CoP_2 on the surface of CdS NRs instead of being doped into the CdS lattice.

The photoluminescence (PL) spectra represent the transfer capacity of photogenerated charge carriers, which is the critical factor to the photocatalytic performance. Fig. 6a presents the PL spectra of Co0-P0 and Co10-P50, distinct emission bands at about 530 nm could be clearly observed, which is characteristic emission spectra of CdS [28]. In addition, the PL intensity of Co10-P50 is much lower than that of Co0-P0. The lower PL intensity represent lower electron-hole recombination efficiency [28]. This explains that electrons excited into the conduction band are bound to live somewhere, impeding the recombination of electron hole pairs. Moreover, as shown in Fig. 6b, the time-resolved photoluminescence (TRPL) spectra of Co0-P0 and Co10-P50 was determined to reveal the lifetime of photogenerated charge carriers. Compared to Co0-P0 (0.54 ns), Co10-P50 showed an obvious increased PL lifetime (0.98 ns), which is almost twice as much as the former. The longer lifetime of charge carriers represents a higher possibility for photogenerated electrons to participate in the reduction
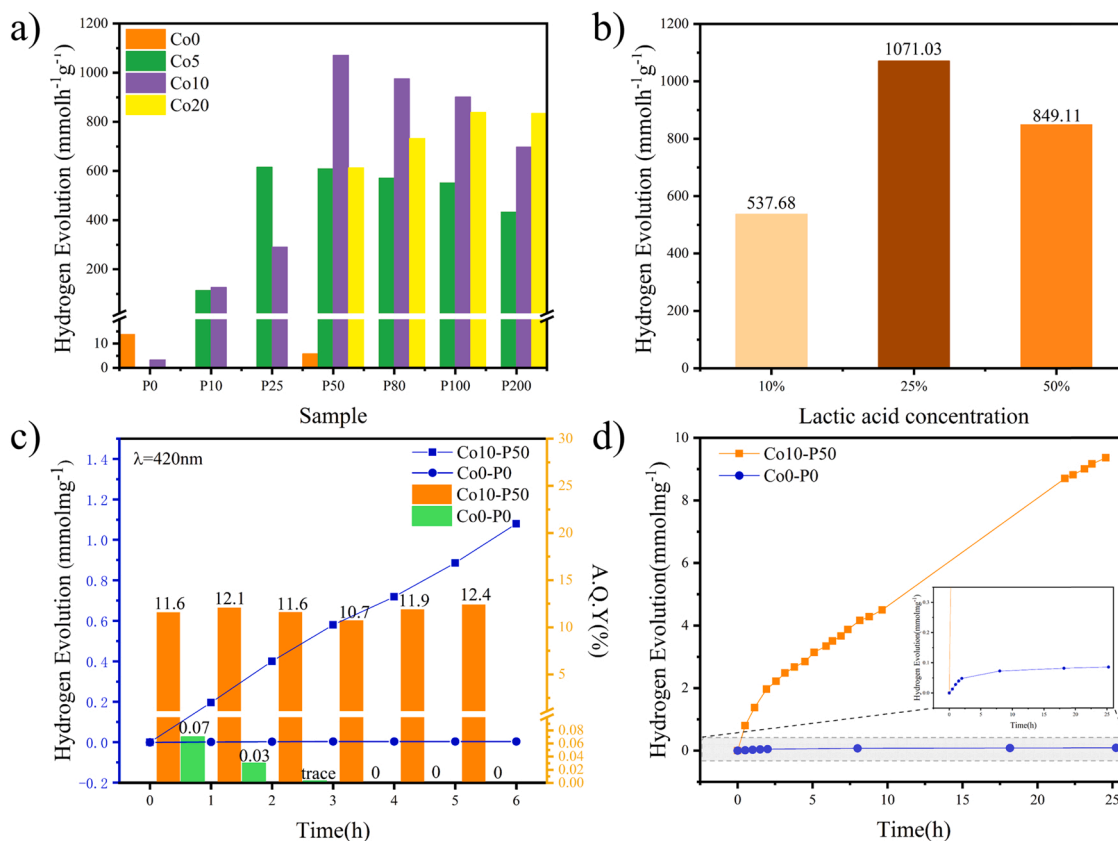
Fig. 4. Photocatalytic activity of Cox-Py under different conditions. a) The rate of hydrogen evolution on Cox-Py (x = 0, 5, 10, 20, and y = 0, 10, 25, 50, 80, 100, 200,) at room temperature. b) The rate of hydrogen evolution on Co10-P50 at different concentrations of the hole scavenger at room temperature. c) The time courses of hydrogen and A.Q.Y. on Co10-P50 and Co0-P0 under monochromatic 420 nm light irradiation. d) Long term evolution of hydrogen for 25 h under visible light irradiation (λ > 420 nm) using Co10-P50 and Co0-P0 at room temperature.
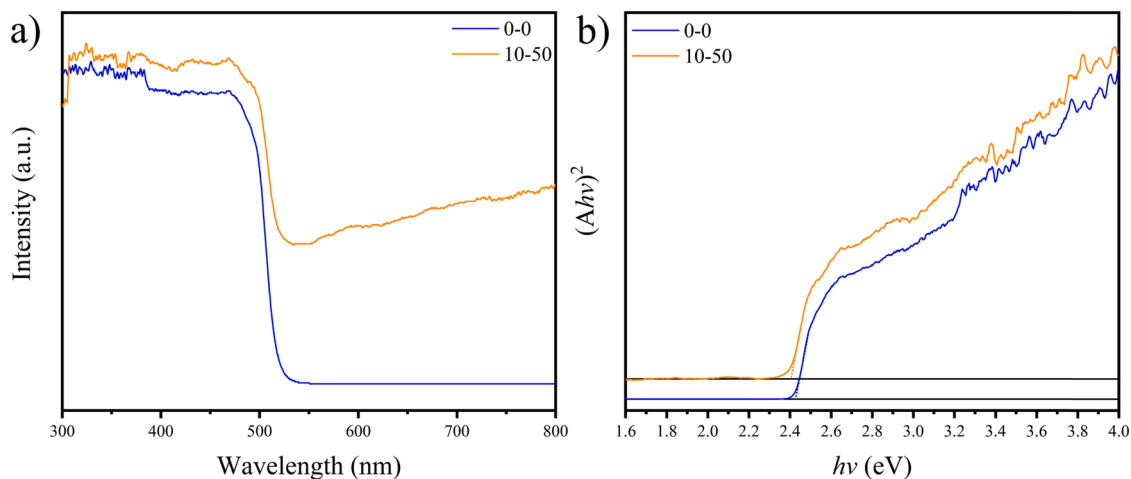

Fig. 5. a) UV–vis DRS of Co0-P0 and Co10-P50. b) Corresponding Kubelka-Munk transformation.

of protons before recombination. Based on the above analysis of fluorescence signal, we get the conclusion that CoP_2 loading improves the mobility and the lifetime of charge carriers. However, in the subsequent electrochemical tests, we got the seemingly "contradictory" results (Fig. 6c and Fig. S6). From Fig. 6c, the EIS signal radius of Co10-P50 is larger than that of Co0-P0 regardless of whether the light is on or off, indicating that Co10-P50 has a larger parallel resistance Rp (here means charge transfer resistance) (Table S1). The reasons for this strange phenomenon will be discussed in more detail later, briefly explained

here. In fact, different from the previously reported heterogeneous interface, the special interface consists of "built-in electric field zone" and "electron trap [47,48] zone" between CoP_2 and CdS NRs produces the phenomenon mentioned above. As a result of built-in electric field, after the electrons are excited to the conduction band, the directional transfer of carriers occurs and the electron-hole pairs can be separated effectively, which inhibit the recombination of electron-hole pairs and prolong the lifetime of carriers, then the electrons are confined to an "electron trap zone". The trapped electrons could not transfer through
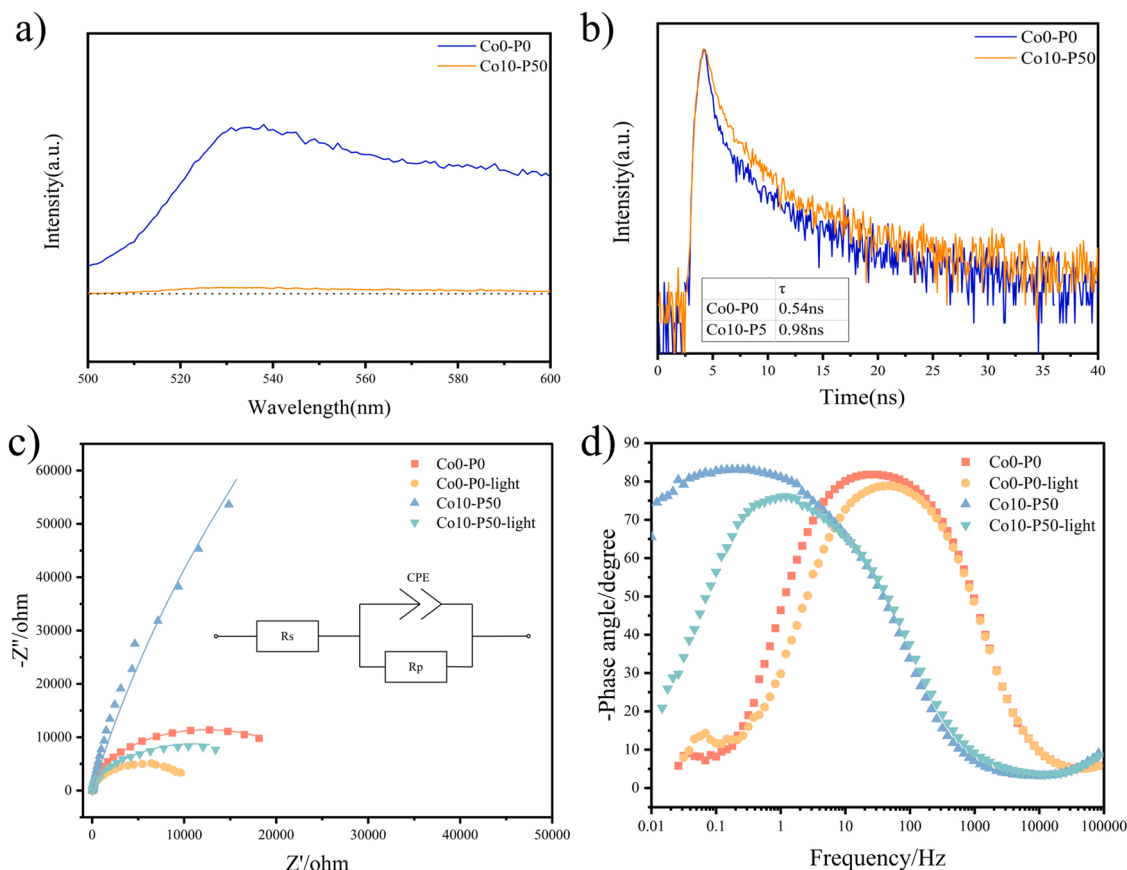
Fig. 6. a) Room-temperature PL spectra of Co0-P0 and Co10-P50. b) Room-temperature TRPL decay curves of Co10-P50 and Co0-P0. c) Nyquist (with equivalent circuit) and d) Bode plots of Co0-P0 and Co10-P50 with and without irradiation.

the bulk of CoP_2 outwards, only migrate along the interface, leading to the reduction of photocurrent intensity (Fig. S6) and the larger radius of EIS signal. In addition, for both Co0-P0 and Co10-P50, irradiation caused a decrease in EIS radius, which was attributed to the fact that photogenerated carriers increase the conductivity of the material and decrease the Rp. In particular, the decrease in the Rp value was more pronounced for Co10-P50, indicating that irradiation leads to more carriers. From Bode plot (Fig. 6d), Co10-P50 has a smaller characteristic frequency, further indicating its longer carrier lifetime [49]. Moreover, irradiation increased the characteristic frequencies of both samples, indicating that electrons and holes tend to recombine easier in materials with high-energy excited states. From the parameters obtained from the equivalent circuit fitting (Table S1), another significant difference between Co10-P50 and Co0-P0 is manifested in CPE-T. The capacitance value of Co0-P0 comes from the double-layer capacitance. While, the relatively much larger capacitance value of Co10-P50 comes from the electron trap formed at the interface, which acts as an electron storage repository. In addition, light did not significantly change the capacitance values of Co0-P0, while significantly decrease the capacitance values of Co10-P50, indicating that the photogenerated electrons were confined in the "electron traps zone", weakening the capacitive effect of the electron traps.

The first-principles calculation based on DFT was conducted to reveal the existence of this special interface mentioned above (Fig. S7). As we all know, CdS is a semiconductor with a direct bad gap, when coupled with CoP_2, the inter part of CdS NRs still keep regular crystal structure and possesses a semiconductor characteristic (Fig. 7a). But as is shown in Fig. 7b, the "metallization" of CdS interface is clearly observed, which caused that the band gap is no longer exist. That may be due to a strong interaction between CdS NRs and CoP_2, which leads to a strong distortion of the surface of CdS NRs. Similarly, CoP_2 is a semiconductor

owns a narrow band gap, which has been proved in this work (Fig. 7c) and another article [50]. When loaded on CdS NRs, the band gap disappears with the increase of electron density of state near the Fermi level, and the energy range of electronic states was broadened (Fig. 7d). Briefly speaking, the "metallization" occurs on the interface of CoP_2, which could increase the conductivity, and therefore, be convenient for electron transfer.

To figure out the evolution of band structure and the formation of the built-in electric field, the work function was calculated and the XPS valence band spectrum was conducted. The work function of CdS (100) plane and CoP_2 ($\bar{2}02$) plane were calculated to be 5.141 eV and 3.911 eV, respectively (Fig. 8a-b, Fig. S8), indicate the Fermi level of CdS NRs and CoP_2 are -5.141 eV and -3.911 eV (the vacuum level is set to be 0 eV), respectively. From the XPS valence band spectrum (Fig. S9), the valence band of CdS NRs is located 0.52 eV below the Fermi level. Combined with UV–vis DRS result, the conduction band of CdS NRs is located 1.91 eV above the Fermi level. For CoP_2, the band edge potential is similar to Fermi energy level, so it is not studied in depth. From Fig. S10, the work function of Co10-P50 after reaching potential equilibrium is 4.16 eV, indicating the Fermi level of the hybrid is -4.16 eV, in which the electrons could be able to reduce protons considering that the H/H^+ redox potential relative to the vacuum level is -4.44 eV [51].

From the above calculation and experimental results, we propose a novel interfacial lateral electron transfer mechanism. Fig. 8c is the schematic diagram of the evolution of band structure. When CoP_2 was loaded on the surface of CdS NRs, electrons would flow from CoP_2 to CdS NRs cause CdS NRs owns a bigger work function. After reaching thermodynamic equilibrium, electrons are accumulated in CdS NRs and CoP_2 owns more positive charge, that also can be proved by XPS measurement. Therefore, the built-in electric field is formed with orientation
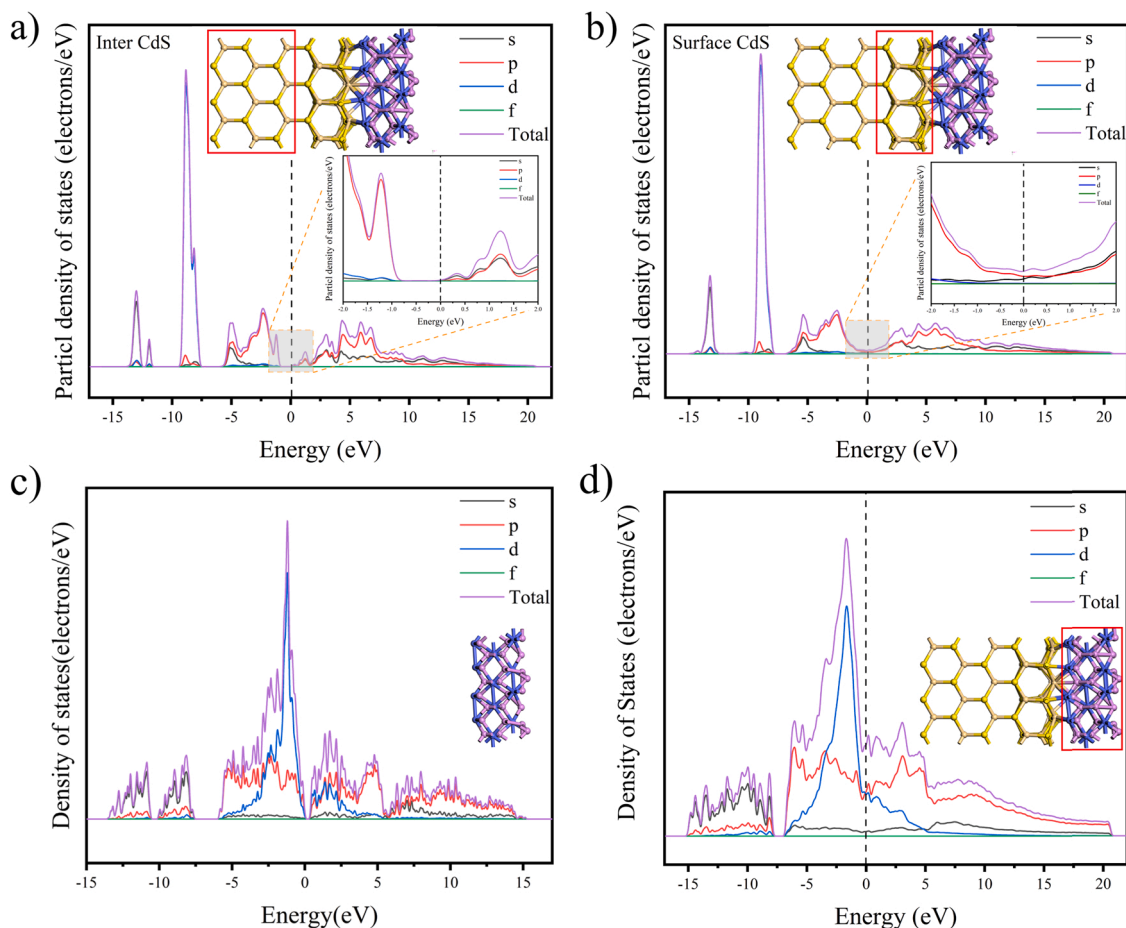
Fig. 7. Density of state distributions of a) inter part of CdS. b) interface part of CdS. c) bulk of CoP_2. d) interface part of CoP_2.

from CoP_2 to CdS. Besides, in such a "built-in electric field zone", there is also an "electron trap zone", in which the electrons can be bound, and the metallized interface serves as a fast channel for electrons to participate in the proton reduction reaction. When the Co10-P50 was illuminated, photo-induced carriers will separate in two opposite directions—electrons migrate to the direction of CoP_2 and holes accumulate in CdS NRs, the holes can be easily consumed by sacrificial agent while the electrons can migrate to the interface between CoP_2 and CdS to participate in hydrogen evolution reaction efficiently.

In fact, the construction of this interfacial lateral electron migration path is not specious. (1) The strong interaction brings about large structural distortion, which significantly changes the distribution of electronic states near the Fermi level and creates a "metallized" interface. (2) CoP_2, as a narrow band gap semiconductor, is easy to be metallized at the interface through interfacial lattice distortion, and a certain band gap can construct electron traps. (3) The proper band structures and Fermi levels of CdS and CoP_2 create favorable band bending, which forms a built-in electric field in the right direction and eventually leads to the desired electron flow.

This new heterostructure of CoP_2/CdS is very different from the traditional heterojunction. (1) the structure is different. The conventional heterojunction is dominated by the built-in electric field, while the new heterostructure additionally includes a certain thickness of metallized interface as an electron trap. (2) The electron migration path is different. Given that the strong electron separation occurs only at the interface, the bulk region away from the interface in the conventional heterojunction lacks sufficient electron migration driving force, and the photogenerated electrons spread randomly after crossing the interface, lowering electron transport efficiency. In contrast, the electron trap in the new heterostructure of CoP_2/CdS can serve to bind electrons, while

the metallic properties of the electron trap itself provide a fast migration channel for electrons. More importantly, the built-in electric field continuously injects photogenerated electrons into the region, providing sufficient drive for electron migration. Moreover, the lattice distortion occurring at the interface tends to make the atomic energy higher and the reactivity of the active sites at the interface is expected to be higher.

4. Conclusion

A novel interfacial lateral electron transfer mechanism is proposed using CoP_2/CdS NRs hybrid composite as a case. CoP_2 has been applied to the photocatalytic hydrogen production system for the first time. Compared to the pristine CdS NRs, the optimal CoP_2/CdS NRs hybrid photocatalyst shows a remarkably improved hydrogen production performance, which reaches 1071 mmol h^{-1} g^{-1} and the A.Q.Y. at 420 nm up to 12 % from 0.07 % of pristine CdS NRs. The improved performance is origin from the strong interface coupling between CoP_2 and CdS NRs, which produced the built-in electric field and, more importantly, "metallized" interface between CoP_2 and CdS NRs, which serves as a unique electron trap that accumulate electrons and promote them transfer along it. The special interface shortens the electron migration distance and make more hot electrons be used efficiently. This work introduces a case that the interface plays a key role to photocatalytic hydrogen production, pointing out that interface engineering is of great significance to improve the photocatalytic hydrogen production performance.

CRediT authorship contribution statement

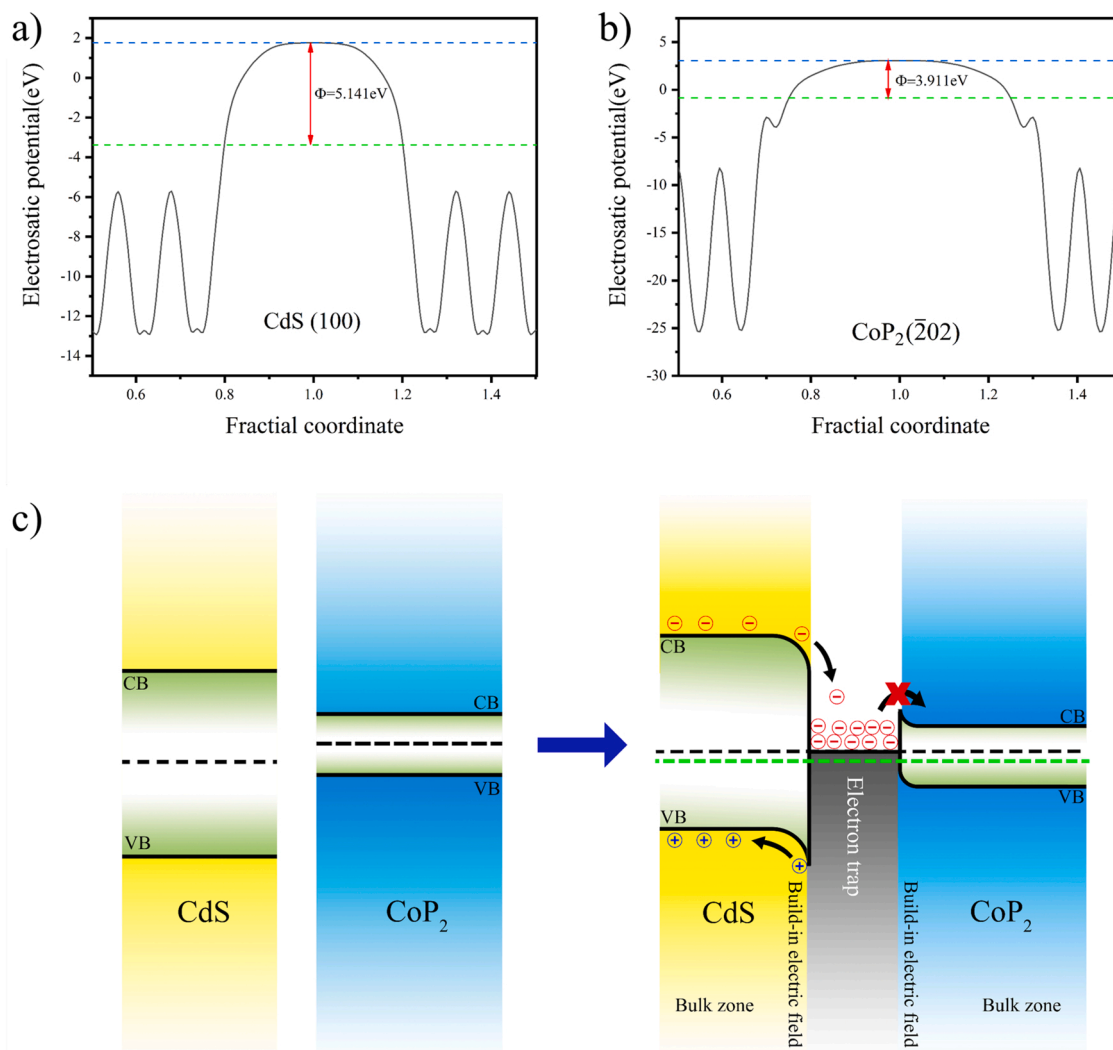**Xiangdong Xue:** Conceptualization, Methodology, Software, Formal

Fig. 8. Calculated electrostatic potentials of a) CdS (100) plane and b) CoP$_2$ ($\overline{2}$02) plane. c) Schematic illustration of the evolution of band structure and charge carrier migration on Co10-P50 under the influence of interface between CdS and CoP$_2$. The green dash line represents the H/H$^+$ potential, the black dash line represents the Fermi level of the materials.

analysis, Investigation, Data curation, Writing – original draft, Visualization. **Wenjun Dong:** Methodology, Validation, Writing – review & editing, Supervision. **Hongyi Gao:** Methodology, Validation, Writing – review & editing, Supervision, Project administration, Funding acquisition. **Qingjie Luan:** Validation, Formal analysis. **Ge Wang:** Conceptualization, Resources, Writing – review & editing, Supervision, Project administration, Funding acquisition.

Declaration of Competing Interest

The authors declare no competing interests.

Data Availability

Data will be made available on request.

Acknowledgments

Appendix A. Supporting information

Supplementary data associated with this article can be found in the online version at doi:10.1016/j.apcatb.2023.122860.

References

[1] A. Fujishima, K. Honda, Electrochemical photolysis of water at a semiconductor electrode, Nature 238 (1972) 37–38.
[2] J. Han, Y. Bian, X. Zheng, et al., A photoelectrochemical cell for pollutant degradation and simultaneous H$_2$ generation, Chin. Chem. Lett. 28 (2017) 2239–2243.
[3] R. Li, Latest progress in hydrogen production from solar water splitting via photocatalysis, photoelectrochemical, and photovoltaic-photoelectrochemical solutions, Chin. J. Catal. 38 (2017) 5–12.
[4] J. Liu, Y. Liu, N. Liu, et al., Metal-free efficient photocatalyst for stable visible water splitting via a two-electron pathway, Science 347 (2015) 970–974.
[5] W. Wang, T. An, G. Li, et al., Earth-abundant Ni$_2$P/g-C$_3$N$_4$ lamellar nanohydrids for enhanced photocatalytic hydrogen evolution and bacterial inactivation under visible light irradiation, Appl. Catal. B: Environ. 217 (2017) 570–580.

[6] P. Zhou, J. Yu, M. Jaroniec, All-solid-state Z-scheme photocatalytic systems, Adv. Mater. 26 (2014) 4920–4935.

[7] J.-P. Zou, L.-C. Wang, J. Luo, et al., Synthesis and efficient visible light photocatalytic H2 evolution of a metal-free g-C3N4/graphene quantum dots hybrid photocatalyst, Appl. Catal. B: Environ. 193 (2016) 103–109.

[8] X. Zou, Y. Zhang, Noble metal-free hydrogen evolution catalysts for water splitting, Chem. Soc. Rev. 44 (2015) 5148–5180.

[9] S. Chen, T. Takata, K. Domen, Particulate photocatalysts for overall water splitting, Nat. Rev. Mater. 2 (2017) 1–17.

[10] T. Hisatomi, K. Domen, Reaction systems for solar hydrogen production via water splitting with particulate semiconductor photocatalysts, Nat. Catal. 2 (2019) 387–399.

[11] K. Takanabe, Photocatalytic water splitting: quantitative approaches toward photocatalyst by design, ACS Catal. 7 (2017) 8006–8022.

[12] Y. Chen, S. Ji, W. Sun, et al., Engineering the atomic interface with single platinum atoms for enhanced photocatalytic hydrogen production, Angew. Chem. Int. Ed. 59 (2020) 1295–1301.

[13] H. He, J. Lin, W. Fu, et al., MoS2/TiO2 edge-on heterostructure for efficient photocatalytic hydrogen evolution, Adv. Energy Mater. 6 (2016), 1600464.

[14] R. Shen, C. Jiang, Q. Xiang, et al., Surface and interface engineering of hierarchical photocatalysts, Appl. Surf. Sci. 471 (2019) 43–87.

[15] H. Zhang, J. Cai, Y. Wang, et al., Insights into the effects of surface/bulk defects on photocatalytic hydrogen evolution over TiO2 with exposed {001} facets, Appl. Catal. B: Environ. 220 (2018) 126–136.

[16] C. Gao, T. Wei, Y. Zhang, et al., A photoresponsive rutile TiO2 heterojunction with enhanced electron–hole separation for high-performance hydrogen evolution, Adv. Mater. 31 (2019), 1806596.

[17] J. Kosco, M. Bidwell, H. Cha, et al., Enhanced photocatalytic hydrogen evolution from organic semiconductor heterojunction nanoparticles, Nat. Mater. (2020) 1–7.

[18] M. Shakeel, M. Arif, G. Yasin, et al., Layered by layered Ni-Mn-LDH/g-C3N4 nanohybrid for multi-purpose photo/electrocatalysis: morphology controlled strategy for effective charge carriers separation, Appl. Catal. B: Environ. 242 (2019) 485–498.

[19] B.-X. Zhou, S.-S. Ding, B.-J. Zhang, et al., Dimensional transformation and morphological control of graphitic carbon nitride from water-based supramolecular assembly for photocatalytic hydrogen evolution: from 3D to 2D and 1D nanostructures, Appl. Catal. B: Environ. 254 (2019) 321–328.

[20] A. Meng, L. Zhang, B. Cheng, et al., Dual cocatalysts in TiO2 photocatalysis, Adv. Mater. 31 (2019), 1807660.

[21] H. Zhang, P. Zhang, M. Qiu, et al., Ultrasmall MoOx clusters as a novel cocatalyst for photocatalytic hydrogen evolution, Adv. Mater. 31 (2019), 1804883.

[22] J. Di, J. Xia, M.F. Chisholm, et al., Defect-tailoring mediated electron–hole separation in single-unit-cell Bi3O4Br nanosheets for boosting photocatalytic hydrogen evolution and nitrogen fixation, Adv. Mater. 31 (2019), 1807576.

[23] Y. Jiang, Z. Sun, C. Tang, et al., Enhancement of photocatalytic hydrogen evolution activity of porous oxygen doped g-C3N4 with nitrogen defects induced by changing electron transition, Appl. Catal. B: Environ. 240 (2019) 30–38.

[24] S. Hua, D. Qu, L. An, et al., Highly efficient p-type Cu3P/n-type g-C3N4 photocatalyst through Z-scheme charge transfer route, Appl. Catal. B: Environ. 240 (2019) 253–261.

[25] X. Lu, J. Xie, X. Chen, et al., Engineering MPx (M= Fe, Co or Ni) interface electron transfer channels for boosting photocatalytic H2 evolution over g-C3N4/MoS2 layered heterojunctions, Appl. Catal. B: Environ. 252 (2019) 250–259.

[26] H.-W. Man, C.-S. Tsang, M.M.-J. Li, et al., Transition metal-doped nickel phosphide nanoparticles as electro-and photocatalysts for hydrogen generation reactions, Appl. Catal. B: Environ. 242 (2019) 186–193.

[27] Z. Sun, M. Zhu, X. Lv, et al., Insight into iron group transition metal phosphides (Fe2P, Co2P, Ni2P) for improving photocatalytic hydrogen generation, Appl. Catal. B: Environ. 246 (2019) 330–336.

[28] Y. Dong, L. Kong, G. Wang, et al., Photochemical synthesis of CoxP as cocatalyst for boosting photocatalytic H2 production via spatial charge separation, Appl. Catal. B: Environ. 211 (2017) 245–251.

[29] J. Wang, P. Wang, C. Wang, et al., In-situ synthesis of well dispersed CoP nanoparticles modified CdS nanorods composite with boosted performance for photocatalytic hydrogen evolution, Int. J. Hydrogen Energy 43 (2018) 14934–14943.

[30] H. Li, X. Yan, B. Lin, et al., Controllable spatial effect acting on photo-induced CdS@ CoP@ SiO2 ball-in-ball nano-photoreactor for enhancing hydrogen evolution, Nano Energy 47 (2018) 481–493.

[31] S. Cao, Y. Chen, C.-J. Wang, et al., Spectacular photocatalytic hydrogen evolution using metal-phosphide/CdS hybrid catalysts under sunlight irradiation, Chem. Commun. 51 (2015) 8708–8711.

[32] W. Bi, L. Zhang, Z. Sun, et al., Insight into electrocatalysts as co-catalysts in efficient photocatalytic hydrogen evolution, ACS Catal. 6 (2016) 4253–4257.

[33] H. Li, P. Wen, D.S. Itanze, et al., Phosphorus-rich colloidal cobalt diphosphide (CoP2) nanocrystals for electrochemical and photoelectrochemical hydrogen evolution, Adv. Mater. 31 (2019), 1900813.

[34] M.C. Payne, M.P. Teter, D.C. Allan, et al., Iterative minimization techniques for ab initio total-energy calculations: molecular dynamics and conjugate gradients, Rev. Mod. Phys. 64 (1992) 1045.

[35] S.J. Clark, M.D. Segall, C.J. Pickard, et al., First principles methods using CASTEP. Zeitschrift für Kristallographie-Crystalline, Materials 220 (2005) 567–570.

[36] W. Kohn, L.J. Sham, Self-consistent equations including exchange and correlation effects, Phys. Rev. 140 (1965) A1133.

[37] J.P. Perdew, K. Burke, M. Ernzerhof, Generalized gradient approximation made simple, Phys. Rev. Lett. 77 (1996) 3865.

[38] D. Vanderbilt, Soft self-consistent pseudopotentials in a generalized eigenvalue formalism, Phys. Rev. B 41 (1990) 7892.

[39] H.J. Monkhorst, J.D. Pack, Special points for Brillouin-zone integrations, Phys. Rev. B 13 (1976) 5188.

[40] X.-P. Wu, L. Gagliardi, D.G. Truhlar, Cerium metal–organic framework for photocatalysis, J. Am. Chem. Soc. 140 (2018) 7904–7912.

[41] X. Wu, C. Lao, Y. Li, et al., Tunable synthesis of CoP and CoP2 decorated 3D carbon Nanohybrids and the application of CoP2 decorated one in electrochemical detection of chloramphenicol in Milk and honey, J. Electrochem. Soc. 165 (2018) B916–B923.

[42] B. Xu, P. He, H. Liu, et al., A 1D/2D helical CdS/ZnIn2S4 nano-heterostructure, Angew. Chem. Int. Ed. 53 (2014) 2339–2343.

[43] W. Jeitschko, U. Flörke, U. Scholz, Ambient pressure synthesis, properties, and structure refinements of VP4 and CoP2, J. Solid State Chem. 52 (1984) 320–326.

[44] Z. Yan, X. Yu, A. Han, et al., Noble-metal-free Ni(OH)2-modified CdS/reduced graphene oxide nanocomposite with enhanced photocatalytic activity for hydrogen production under visible light irradiation, J. Phys. Chem. C 118 (2014) 22896–22903.

[45] Y. Zhou, Y. Yang, R. Wang, et al., Rhombic porous CoP2 nanowire arrays synthesized by alkaline etching as highly active hydrogen-evolution-reaction electrocatalysts, J. Mater. Chem. A 6 (2018) 19038–19046.

[46] J. Low, B. Dai, T. Tong, et al., In situ irradiated X-ray photoelectron spectroscopy investigation on a direct Z-scheme TiO2/CdS composite film photocatalyst, Adv. Mater. 31 (2019), 1802981.

[47] X. Qu, M. Liu, Z. Gao, et al., A novel ternary Bi4NbO8Cl/BiOCl/Nb2O5 architecture via in-situ solvothermal-induced electron-trap with enhanced photocatalytic activities, Appl. Surf. Sci. 506 (2020), 144688.

[48] H.-Q. Xu, J. Hu, D. Wang, et al., Visible-light photoreduction of CO2 in a metal–organic framework: boosting electron–hole separation via electron trap states, J. Am. Chem. Soc. 137 (2015) 13440–13443.

[49] R. Bariki, D. Majhi, K. Das, et al., Facile synthesis and photocatalytic efficacy of UiO-66/CdIn2S4 nanocomposites with flowerlike 3D-microspheres towards aqueous phase decontamination of triclosan and H2 evolution, Appl. Catal. B: Environ. 270 (2020), 118882.

[50] Z. Yang, L. Liu, X. Wang, et al., Stability and electronic structure of the Co–P compounds from first-principle calculations, J. Alloy. Compd. 509 (2011) 165–171.

[51] F. Guo, W. Shi, C. Zhu, et al., CoO and g-C3N4 complement each other for highly efficient overall water splitting under visible light, Appl. Catal. B: Environ. 226 (2018) 412–420.